

# Coherent Electronic and Nuclear Dynamics for Charge Transfer in 1-Ethyl-4-(carbomethoxy)pyridinium Iodide<sup>†</sup>

Andrew M. Moran, Sungham Park,<sup>‡</sup> and Norbert F. Scherer\*

Department of Chemistry and the James Franck Institute, The University of Chicago, 5735 South Ellis Avenue, Chicago, Illinois 60637

Received: March 31, 2006; In Final Form: June 26, 2006

Although polaronic interactions and states abound in charge transfer processes and reactions, quantitative and separable determination of electronic and nuclear relaxation is still challenging. The present paper employs the amplitudes, polarizations, and phases of four-wave mixing signals to obtain unique dynamical information on relaxation processes following photoinduced charge transfer between iodide and 1-ethyl-4-(carbomethoxy)-pyridinium ions. Pump–probe signal amplitudes reveal the coherent coupling of an underdamped 115 cm<sup>−1</sup> nuclear mode to the charge transfer excitation. Assignments of this recurrence to intramolecular vibrational modes of the acceptor and to modulation of the intermolecular donor–acceptor distance are discussed on the basis of a high-level density functional theory normal-mode analysis and previously observed wave packet dynamics of solvated molecular iodine. Nuclear relaxation of the acceptor induces sub-picosecond decay of the pump–probe polarization anisotropy from an initial value of 0.4 to an asymptotic value of −0.05. Electronic structure calculations suggest that relaxation along the torsional coordinate of the ethyl group is the origin of the anisotropy decay. Electric-field-resolved transient grating (EFR-TG) signal fields are obtained by spectral interferometry with a diffractive optic based interferometer. These measurements show that the signal phase and amplitude possess similar dynamics. Model calculations are used to demonstrate how the EFR-TG signal phase yields unique information on transient material resonances located outside the laser pulse spectrum. This effect can be rationalized in that the real and imaginary parts of the nonlinear polarization are related by the Kramers–Kronig transformation, which allows the dispersive component of the polarization response to exhibit spectral sensitivity over a larger frequency range than that defined by the absorption bandwidth.

## I. Introduction

Electron transfer phenomena are pervasive in chemistry, biological function, and the emerging area of molecular electronics.<sup>1–11</sup> Conduction in “molecular wires”,<sup>7–11</sup> charge carrier transport in electroluminescent devices,<sup>12–16</sup> and large quantum yield (but modest thermodynamic efficiency) in photosynthesis<sup>17–19</sup> are all affected or even governed by electron–phonon interactions. Tuning this coupling can lead to optimization of electron transfer behavior. Another important issue is the use of charges to facilitate this tuning or to dope conjugated molecular systems (e.g., polyacetylene, polyaniline) to create semiconducting materials. Knowledge of vibronic coupling is critical to understanding the optical and functional properties of photoresponsive systems such as the retinal chromophore in rhodopsin.<sup>20–22</sup> Further insight into local charge–molecule (polaronic) interactions in this wide range of systems would benefit from more insightful and detailed spectroscopic studies.

The properties of interest in studies of electronic relaxation following photoinduced electron transfer include the electronic coupling of the donor and acceptor, reorganization energy of the solvent, and nuclear mode-specific reorganization energies of the intracomplex coordinates. In verifying quantum correc-

tions to earlier semiclassical theories,<sup>23–25</sup> the mode-specific reorganization energies have recently been investigated.<sup>26–31</sup> However, the strong dependence of the charge transfer rate on both electronic and nuclear contributions makes experimental extraction of various parameters in the rate expression difficult. For example, the electronic coupling matrix element is known to depend on the effective separation between the donor and acceptor states,<sup>32,33</sup> but this distance is not well-defined when it is on the sub-nanometer scale as in an ion pair that exhibits a charge transfer absorption band. Therefore, it is desirable to design experiments in which electronic and nuclear relaxation processes are separable.

The chemical system considered here is a prototypical bimolecular ion pair charge transfer complex, 1-ethyl-4-(carbomethoxy)pyridinium iodide (ECMPI, Figure 1). Many pyridinal cations are effective electron acceptors and have been used extensively for studies of electron transfer due to the favorable stability of their reduced forms (i.e., radicals).<sup>34–36</sup> Ion pair complexes generally have spatially localized, weakly coupled donor and acceptor states, which allows their relaxation dynamics to be described with nonadiabatic rate formulas.<sup>1,3,37</sup> Values for parameters of the rate expression may be obtained and connected to the physical properties of ion pair complexes. These structure–function relationships can then be used for design of more complex systems that are useful for practical applications.

In this paper, electronic and nuclear relaxation dynamics of ECMPI following photoinduced charge transfer are investigated

<sup>†</sup> Part of the special issue “Charles B. Harris Festschrift”.

\* To whom correspondence should be addressed. E-mail: nscherer@uchicago.edu.

<sup>‡</sup> Present address: Department of Chemistry, Stanford University, Stanford, CA 94305.

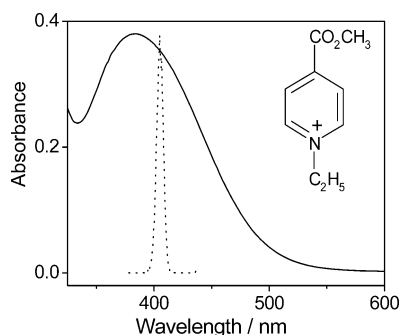


**Figure 1.** Linear absorption spectrum (solid line) for the charge transfer band of ECMPI and the spectrum of the laser pulses (dotted line) used in the experiments. The structure of the 1-ethyl-4-(carbomethoxy)pyridinium cation is shown in the inset. The extinction coefficient of ECMPI is estimated to be  $138 \text{ M}^{-1} \text{ cm}^{-1}$ .<sup>39</sup>

with pump–probe and electric-field-resolved transient grating (EFR-TG) spectroscopies. The goal of this study is to examine the interplay between electronic and nuclear relaxation dynamics in a well-defined but weakly coupled charge transfer system. ECMPI is well-suited to this study because of its simple structure and significant charge redistribution upon electron transfer.<sup>38</sup> Our application of a novel experimental technique to this class of molecular systems is beneficial for meeting the aforementioned challenge. As seen in Figure 1, ECMPI exhibits a broad charge transfer absorption band centered near 400 nm, which has an extinction coefficient of  $\epsilon \approx 138 \text{ M}^{-1} \text{ cm}^{-1}$ .<sup>39</sup> For a pump–probe experiment in which the charge transfer transition is pumped, the transient absorption of the 1-ethyl-4-(carbomethoxy)pyridine radical is strong ( $\epsilon \approx 4300 \text{ M}^{-1} \text{ cm}^{-1}$ )<sup>34</sup> compared to the bleach of the charge transfer band. These aspects of ECMPI allow a more straightforward interpretation of a one-color pump–probe experiment, as the bleach of the charge transfer band can be neglected in the analysis. Furthermore, the use of replica pump and probe pulses is desirable for ECMPI because a relatively long pump–probe beam interaction length ( $\sim 250 \mu\text{m}$ ) is used to compensate for these small extinction coefficients. Poor time resolution would be obtained in a two-color experiment with this path length because of group velocity mismatch. The dipole moments for the ground state of ECMPI and the charge transfer excited state are estimated to be orthogonal.<sup>38</sup> ECMPI should therefore exhibit significant nuclear relaxation due to charge redistribution in the excited state. We observe recurrences in the pump–probe signals for ECMPI, which are interpreted as originating from underdamped nuclear relaxation. Furthermore, signatures of overdamped nuclear relaxation dynamics are found by measuring pump–probe signals for different tensor elements. Finer details of the photophysics are investigated with novel EFR-TG experiments.

Background on the technique and the information content of EFR-TG spectroscopy is given in the following section. A formal description of pump–probe and EFR-TG spectroscopies is presented in section III. The notation and equations given in this section are used to define our measurements. Experimental and computational methods are described in section IV. Our results are presented in section V. An analytical model and calculation are given in section VI to demonstrate the unique sensitivity of the signal phase to transient material resonances. We conclude this paper in section VII by summarizing the important results of this work and their significance.

## II. Background on EFR-TG Spectroscopy

Advances in diffractive optics technology have recently allowed heterodyne detection to be implemented in four-wave mixing spectroscopies at optical frequencies.<sup>40–44</sup> Previous diffractive optics based transient grating experiments utilized a wavelength-integrated method of heterodyne detection in which the signal field is only partially resolved.<sup>42,45</sup> Here, and in other recent work,<sup>46,47</sup> we use spectral interferometry to completely resolve the electric fields of transient grating signals. The additional information is given by the signal phase. The information content of the signal phase may be understood in the context of the conventional pump–probe method, which provides the absorptive projection of the signal field. In pump–probe spectroscopy, a pump pulse is absorbed by a resonant system to produce a transient nonequilibrium state. Relaxation of this nonequilibrium state is interrogated by measuring the transient transmission of a probe pulse at various delays after the pump pulse arrives at (i.e., interacts with) the sample. To measure transient changes in electronic resonance structure in various spectral regions, the color of the probe pulse must be tuned to the region of interest. This constitutes a principal limitation of the pump–probe method; information on photo-induced changes in material resonances are constrained by the bandwidth of the probe pulse.

In contrast, the signal phase is sensitive to resonances in spectral regions that exceed the bandwidth of the probe pulse. This property of the signal phase may be understood by considering the Kramers–Kronig relation between the real and imaginary parts of the third-order polarization, which is exact for delta function pulses. Thus, the information provided by EFR-TG is similar to that obtained by pump–probe spectroscopy with a hole-burning pulse configuration, where dynamics induced by a relatively narrowband pump pulse are monitored with a broadband continuum probe pulse.<sup>48–50</sup> For the present application, the signal phase should be particularly sensitive to the presence of various relaxation channels.

The information content of transient grating spectroscopy has been discussed in the context of frequency dependent amplitude and phase gratings.<sup>51</sup> More recently, Jonas and co-workers stated the relationship between transient grating signal field and photon echo spectra with the projection-slice theorem of Fourier transforms.<sup>52</sup> They later commented on the relationship between the relaxation of dispersive photon echo spectra and the changes in the transient absorption spectrum at frequencies outside the laser pulse bandwidth.<sup>53</sup> The absorptive and dispersive projections of the transient grating signal field were used to reveal the presence of a hot ground state for Crystal Violet.<sup>42</sup> This work is a good example of how the signal phase may be more sensitive than the amplitude to details of an electronic relaxation mechanism.

## III. Principles of Spectroscopic Methods

Expressions for pump–probe and EFR-TG signals are developed in this section in the context of the present experiments. First, the general relation between the third-order source polarization and the four-wave mixing signal is presented. Next, the pump–probe signal is defined as the absorptive projection of the four-wave mixing signal. An expression is then given for the EFR-TG signal, which is valid for detection with spectral interferometry.

**A. Third-Order Spectroscopies.** The general four-wave mixing pulse configuration is shown in Figure 1. In transient grating experiments, pulses 1 and 2 arrive to the sample at the

same time, that is,  $\tau = 0$ . This external electric field may be written as<sup>54</sup>

$$E(\mathbf{r}, t) = \sum_{j=1}^4 \sum_{\nu=1}^3 [E_{j\nu}(\mathbf{k}_j, t) + E_{j\nu}^*(\mathbf{k}_j, t)] \quad (1)$$

where

$$E_{j\nu}(\mathbf{k}_j, t) = \epsilon_{j\nu}(t - \bar{\tau}_j) \exp[i\mathbf{k}_j \cdot \mathbf{r} - i\bar{\omega}_j t - i\phi_{j\nu}(t)] \quad (2)$$

Here,  $\epsilon_{j\nu}(t - \bar{\tau}_j)$  is a slowly varying envelope function for pulse  $j$  centered at time  $\bar{\tau}_j$  with carrier frequency  $\bar{\omega}_j$ , polarization  $\nu$ , wavevector  $\mathbf{k}_j$ , and temporal phase function  $\phi_{j\nu}(t)$ . The frequency domain electric field is given by

$$\tilde{E}_{j\nu}(\mathbf{k}_j, \omega) = \int_{-\infty}^{\infty} dt E_{j\nu}(\mathbf{k}_j, t) \exp(-i\omega t) \quad (3)$$

where  $\tilde{E}_{j\nu}(\mathbf{k}_j, \omega)$  is centered at  $\omega = 0$  because  $E_{j\nu}(\mathbf{k}_j, t)$  is complex. We choose to shift  $\tilde{E}_{j\nu}(\mathbf{k}_j, \omega)$  by  $\bar{\omega}_j$  so that the frequency domain electric fields given in this paper,  $E_{j\nu}(\mathbf{k}_j, \omega)$ , are centered at their carrier frequencies.<sup>46,55</sup> We define  $E_{j\nu}(\mathbf{k}_j, \omega)$  by

$$E_{j\nu}(\mathbf{k}_j, \omega) = \tilde{\xi}_{j\nu}(\omega) \exp[i\mathbf{k}_j \cdot \mathbf{r} + i\varphi_{j\nu}(\omega)] \quad (4)$$

where  $\varphi_{j\nu}(\omega)$  is the spectral phase and  $\tilde{\xi}_{j\nu}(\omega)$  is the real spectral amplitude.

For the transient grating and pump–probe techniques, the nonlinear polarization induced by pulses 1–3 may be expressed as

$$\begin{aligned} P_i^{(3)}(\mathbf{k}_s, t, T) = & \int_0^\infty dt_3 \int_0^\infty dt_2 \int_0^\infty dt_1 R_{ijkl}^{(3)}(t_3, t_2, t_1) \\ & \times E_{3j}(\mathbf{k}_3, t - t_3) \times E_{2k}(\mathbf{k}_2, t - t_3 - t_2) \\ & \times E_{1l}^*(\mathbf{k}_1, t - t_3 - t_2 - t_1) \end{aligned} \quad (5)$$

where  $ijkl = x, y, z$  represent molecular frame polarization components and the third-order impulse response function,  $R_{ijkl}^{(3)}(t_3, t_2, t_1)$ , is a fourth-rank tensor.<sup>56</sup> Transient grating and pump–probe signal wavevectors are given by  $\mathbf{k}_s = -\mathbf{k}_1 + \mathbf{k}_2 + \mathbf{k}_3$ . Under perfect phase-matching conditions, the signal field,  $E_{sv}(\mathbf{k}_s, t, T)$ , is related to the third-order polarization by<sup>56</sup>

$$E_{sv}(\mathbf{k}_s, t, T) = \frac{i2\pi l \omega_l}{n(\omega_l)c} P_v^{(3)}(\mathbf{k}_s, t, T) \quad (6)$$

where  $n(\omega_l)$  is the refractive index of the sample,  $l$  is the optical path length,  $c$  is the speed of light, and  $T$  is the experimentally controlled delay between the 1–2 pulse pair and pulse 3.

**B. Pump–Probe Spectroscopy.** The pump–probe configuration consists of two pulses. To consider the experiment on the same footing as the EFR-TG experiments, we take the pump field to be  $E_{1\nu}^{\text{pu}}(\mathbf{k}_{\text{pu}}, t) = E_{1\nu}^*(\mathbf{k}_1, t) + E_{2\nu}(\mathbf{k}_2, t)$ , where  $-\mathbf{k}_1 = \mathbf{k}_2$ . The probe field is then expressed as  $E_{3\nu}^{\text{pr}}(\mathbf{k}_{\text{pr}}, t) = E_{3\nu}(\mathbf{k}_1, t)$ . The probe pulse has the same wavevector as the signal ( $\mathbf{k}_s = \mathbf{k}_{\text{pr}}$ ) and serves as the local oscillator (no pulse 4). Consequently, the pump–probe technique is sensitive only to the absorptive component of the signal (see eq 6), which is in phase with the probe field and has the same polarization. The  $ijkl = x, y, z$  polarization components in eq 5 refer to the coordinate system of the molecule and must be transformed to obtain the lab frame signals. We denote the lab frame coordinates with the capital letters X, Y, and Z. The lab frame pulse polarizations may be decomposed into two components, Y and Z, when the pump

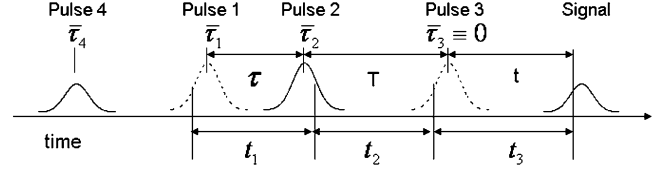


**Figure 2.** General four-wave mixing pulse sequence. Arrival times of the laser pulse peaks are represented by  $\{\bar{\tau}_i\}$ . The delays,  $\tau = \bar{\tau}_2 - \bar{\tau}_1$  and  $T = \bar{\tau}_3 - \bar{\tau}_2$ , are experimentally controlled.  $T$  is varied and  $\tau = 0$  is fixed in EFR-TG experiments. Intervals between field-matter interaction times are given by  $t_1, t_2$ , and  $t_3$ . The zero of time,  $t$ , is defined as when the peak of pulse 3 arrives to the sample, i.e.,  $\bar{\tau}_3 = 0$  fs. The delay of pulse 3 with respect to pulse 4 is fixed ( $\bar{\tau}_3 - \bar{\tau}_4 = 700$  fs).

and probe propagate in the X direction. When the pump is polarized in the Z direction, the pump–probe signals can be written as

$$S_{ZZZZ}(T) = \int_{-\infty}^{\infty} dt E_{sZ}(\mathbf{k}_s, t, T) E_Z^{\text{pr}}(\mathbf{k}_3, t) \quad (7a)$$

$$S_{YYZZ}(T) = \int_{-\infty}^{\infty} dt E_{sY}(\mathbf{k}_s, t, T) E_Y^{\text{pr}}(\mathbf{k}_3, t) \quad (7b)$$

Equation 7 assumes that the spectrum of the probe exhibits negligible changes in intensity and shape upon transmission through the sample. However, the fractional change in transmittance,  $\Delta T/T$ , reported here is not sensitive to the absolute intensity of the probe pulse. It is useful to consider linear combinations of these tensor elements to monitor electronic relaxation processes. For completeness, the pump–probe anisotropy is defined as

$$r(T) = \frac{S_{ZZZZ}(T) - S_{YYZZ}(T)}{S_{ZZZZ}(T) + 2S_{YYZZ}(T)} \quad (8)$$

**C. Electric-Field-Resolved Transient Grating.** EFR-TG signals fields are obtained by spectral interferometry.<sup>57–60</sup> The total heterodyne detected interference spectrum,  $I_{\text{tot}}(\omega_t, T, \bar{\tau}_4)$ , is given by<sup>55,61,62</sup>

$$I_{\text{tot}}(\omega_t, T, \bar{\tau}_4) = \left| \int_{-\infty}^{\infty} dt [E_s(t, T) + E_4(t - \bar{\tau}_4)] \exp(i\omega_t t) \right|^2 \quad (9)$$

where  $E_s(t, T)$  is defined in eq 6. We note that  $\omega_t$  is conjugate to  $t$ , where  $t = 0$  is defined as the time the peak of the probe pulse arrives at the sample (see Figure 2). Indices for pulse polarizations are omitted in this section, as the EFR-TG experiments are all performed with magic angle polarizations (see below). Furthermore, all expressions assume the general transient grating pulse configuration, where pulses 1 and 2 arrive to the sample at the same time. The total detected intensity in eq 9 is Fourier transformed, allowing the signal and local oscillator intensities,  $|E_s(t, T)|^2 + |E_4(t - \bar{\tau}_4)|^2$ , to be removed in the time domain. The complex cross term of eq 9 is then expressed as<sup>46,63</sup>

$$I_{\text{het}}[\omega_t, T; \psi(\omega_t)] = \hat{\xi}_s(\omega_t, T) \hat{\xi}_4(\omega_t) \exp\{i[\psi(\omega_t) - \omega_t \bar{\tau}_4]\} \quad (10)$$

where  $\hat{\xi}_j(\omega_t, T, \tau) = \xi_j(\omega_t, T, \tau) \exp[i\mathbf{k}_j \cdot \mathbf{r}]$  and  $\psi(\omega_t)$  is the phase difference between the signal and local oscillator,  $\psi(\omega_t) = \varphi_s(\omega_t) - \varphi_4(\omega_t)$ . The signal field is isolated by obtaining values for two parameters of eq 10: the delay,  $\bar{\tau}_4$ , is acquired by Fourier transforming an interference spectrum of field 3 and the local oscillator (field 4); the power spectrum of the local oscillator,  $|\xi_4(\omega_t)|^2$ , is measured while pulses 1–3 are blocked. The phase



of the local oscillator,  $\varphi_4(\omega_t)$ , is calibrated by performing an EFR-TG experiment with neat acetonitrile. Acetonitrile is transparent at 405 nm, and therefore, the signal is predominantly dispersive.<sup>42,46</sup> Dividing eq 10 by  $\hat{\xi}_4(\omega_t)$  and  $\exp(-i\omega_t\bar{\tau}_4)$  and then adding  $\varphi_4(\omega_t)$  to  $\psi(\omega_t)$  gives the heterodyne detected EFR-TG signal field

$$E_s(\omega_t, T) = \hat{\xi}_s(\omega_t, T) \exp[i\varphi_s(\omega_t)] \quad (11)$$

In parametrizing  $\varphi_s(\omega_t)$  of eq 11, we follow the sign convention used by others.<sup>43,44,52,64</sup> The phase of the signal for neat acetonitrile at  $T = 0$  is taken to be  $\pi/2$ . Therefore, the imaginary component of eq 11 is positive for solvent emission. This also means that the real component of the signal associated with transient photobleaching (absorption) of a resonant system is positive (negative), the same sign as the transmission change.

#### IV. Methods

**A. Electronic Structure Calculations.** All calculations were performed with the Gaussian 2003 suite of programs.<sup>65</sup> Ground state equilibrium structures of the 1-ethyl-4-(carbomethoxy)pyridinium (+1) cation and the neutral radical were computed at the B3LYP/6-311G(d,p) level. To calculate the equilibrium structure of the ECMPI complex, the internal coordinates of 1-ethyl-4-(carbomethoxy)pyridinium cation were frozen at the B3LYP/6-311G(d,p) minimum and the position of the iodide ion was optimized at the B3LYP/Lanl2DZ level. The Lanl2DZ basis set was used to compute the equilibrium geometry of the complex due to failure of self-consistent field convergence at higher levels of theory. The linear absorption spectra for ECMPI and the neutral 1-ethyl-4-(carbomethoxy)pyridine radical were computed with the CIS/Lanl2DZ and CIS/6-311+G(d) methods, respectively. The transition density cube algorithm was used to compute transition densities on a three-dimensional grid in real space.<sup>66</sup> Plots were generated with Molden.<sup>67</sup>

**B. Experiment.** Most of the data presented in this paper were collected using a home-built 1 kHz amplified Ti:sapphire laser system.<sup>46</sup> A second home-built, high-repetition-rate (10–250 kHz) system<sup>68</sup> producing shorter pulses (35 fs) was used to perform a pump–probe measurement from which fitting parameters were extracted (see Figure 8 below). In all experiments, the second harmonic of the laser system fundamental was generated by focusing a portion of the beam into a 200  $\mu\text{m}$  thick BBO crystal. The second-harmonic beam was double-passed through a prism pair to obtain compressed pulses at the sample position.

Pump–probe anisotropy data were collected with the following procedure. Polarizers (Karl Lambrecht) were oriented in the pump and probe beams prior to the sample to obtain well-defined polarizations. A half-waveplate (Karl Lambrecht) was placed in the path of the pump beam between the polarizer and the sample and rotated to measure different tensor elements. Data for the  $S_{zzzz}(T)$  and  $S_{yyzz}(T)$  tensor elements were collected by performing five scans ( $\sim 90$  s/scan) for one tensor element and then rotating the polarization of the pump beam with the half-waveplate to record the signal for the other tensor element. Twenty scans for each tensor element were obtained by repeating this process four times. An optical Kerr effect measurement was performed with neat  $\text{CCl}_4$  before and after the experiment to ensure that time zero had not drifted. The sample was contained in a 1 mm path length flow cell with an optical density of 0.3 at 400 nm, and the total sample volume was 25 mL. The full sample volume was replaced with an identical solution after 30 min. We found that the linear

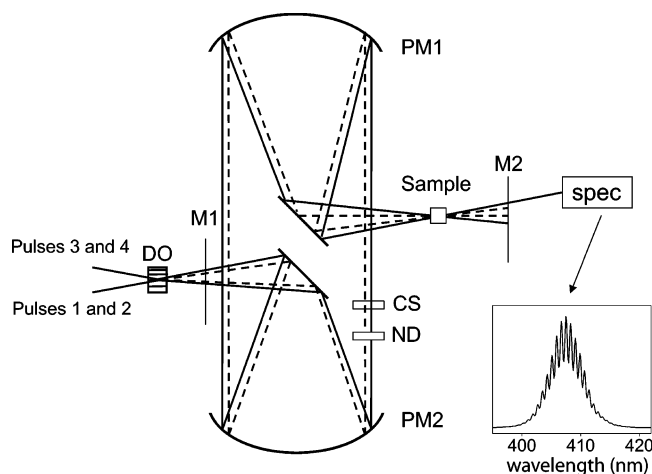


**Figure 3.** Setup used for EFR-TG spectroscopy. Two pulse pairs are created at the diffractive optic (DO): pulses 1 and 2 (pump); pulse 3 (probe) and pulse 4 (local oscillator). Solid and dashed lines represent displacement in height. PM1 and PM2 are aluminum coated, 17.5 in. focal length on-axis parabolic mirrors. Masks spatially isolate the  $\pm 1$  diffraction order beams before the sample (M1) and the collinear signal and LO after the sample (M2). The signal,  $E_s(t)$ , and LO,  $E_4(t - \bar{\tau}_4)$ , interfere in a spectrometer (spec) to give an interference spectrum. The local oscillator is attenuated using a neutral density filter (ND). Pulse 3 is delayed with respect to the local oscillator by  $\approx 700$  fs using glass cover slips, that is,  $\bar{\tau}_4 \approx -700$  fs.

absorption spectrum and pump–probe signals for solutions of ECMPI change substantially after  $\sim 60$  min of exposure to the laser pulses. The pump (200 nJ) and probe (20 nJ) were focused into the sample with a 200 mm focal length lens. The probe beam was directed through a polarizer (Karl Lambrecht) after the sample, and the signal was detected with a PMT (Hamamatsu). Signals were processed with a lock-in amplifier (Stanford Research, SR-830) referenced to a chopper in the pump beam and sampled 1000 times at each delay step with a 16-bit ADC (National Instruments). The probe signal was divided by that of the reference, which was derived by low pass filtering the probe signal to give the fractional change of the transmitted probe intensity,  $\Delta T/T$ . This signal detection scheme resulted in better than one part in  $10^6$  sensitivity. The temporal instrument response for the 400 nm–400 nm pump–probe experiments was 125 fs, as determined by cross-correlation of the pump and probe pulses in  $\text{CCl}_4$ .

EFR-TG measurements are performed using the diffractive optics based interferometer shown in Figure 3.<sup>46</sup> Heterodyne detection of the EFR-TG signal requires stable phase differences between the 1–2 and 3–4 field pairs (Figure 2). This phase stability is achieved by deriving these two field pairs from the  $\pm 1$  diffraction orders of two laser pulses incident on the diffractive optic (Holoeye Photonics). The resulting boxcar pattern is imaged onto the sample with a combination of on-axis parabolic mirrors (Edmund, 17.5 in. focal lengths). Measurements of the passive phase stability for this interferometer result in a standard deviation of 0.14 rad over 4 h.

The energies for pulses 1 and 2 are both 40 nJ, whereas that of pulse 3 is 10 nJ. All EFR-TG signals were acquired with the polarizations of fields 1 and 2 oriented at  $54.7^\circ$  with respect to fields 3 and 4. The local oscillator is attenuated by 3–4 orders of magnitude with a neutral density filter and precedes pulse 3 by 700 fs. The full width at half-maximum (fwhm) spot size of each beam at the sample was  $\sim 60 \mu\text{m}$ . The  $T = 0$  delay between the 1–2 pulse pair and pulse 3 is determined by fitting the amplitude of a transient grating measurement with neat  $\text{CCl}_4$  to a Gaussian function.  $\text{CCl}_4$  is used for this purpose because

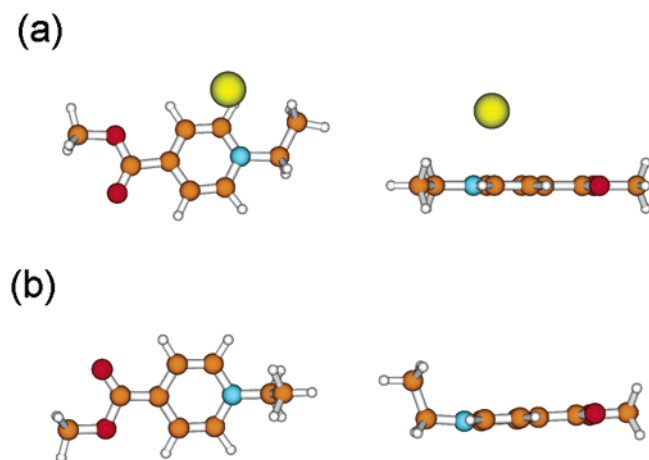


**Figure 4.** Equilibrium geometries for (a) the ECMPI complex and (b) the radical at the equilibrium geometry of the radical. See section IIIA for details on the procedures used to obtain these structures. The yellow sphere is  $I^-$ , orange = C, red = O, blue = N, white = H.

the response is dominated by its quasi-instantaneous electronic nonlinearity.<sup>69</sup>

The EFR-TG signal and local oscillator pulses, which are collinear after the sample, are focused into a 0.32 m monochromator (Jobin-Yvon TRIAX 320) and dispersed with a 600 g/mm grating (blazed at 450 nm) on a charge coupled device array detector (Hamamatsu S7032-1007). The signals are integrated for 3 s before being read out in line binning mode (6 ms). The interference spectrum between the local oscillator and the EFR-TG signal is processed by Fourier transform algorithms.<sup>57–60</sup> Spectral interferometry is capable of determining the spectral phase of the signal up to a constant term. We extract the absolute phase of the signal by calibrating the phase of the local oscillator (see section IIIC) using an EFR-TG measurement with neat acetonitrile. The sample cell is not moved between this calibration measurement and the experiment with the ECMPI solution.

The salt, 1-ethyl-4-(carbomethoxy)pyridinium iodide (Sigma-Aldrich), was used without further purification. The solids were dissolved in spectrophotometric grade acetonitrile (Fisher), termed MeCN.

## V. Results

**A. Electronic Structure Calculations.** The calculated equilibrium geometry for ECMPI is shown in Figure 4a. The structure of the 1-ethyl-4-(carbomethoxy)pyridinium cation in the ECMPI ion pair is planar with the heavy atoms of the  $-C_2H_5$  and  $-CO_2CH_3$  groups located in the plane of the aromatic ring. The iodide ion is located 3.7 Å from the nitrogen atom. Geometry optimizations at the HF/Lanl2DZ and B3LYP/Lanl2DZ levels gave almost identical equilibrium configurations for ECMPI. We did not find a potential energy minimum for a more symmetrical position of the iodide ion with respect to the cation by optimizing from several different initial configurations. As seen in Figure 4b, the major difference between the equilibrium geometries of the cation and the 1-ethyl-4-(carbomethoxy)pyridine radical is that the  $-C_2H_5$  group is located in the plane of the ring for the cation but points  $\sim 90^\circ$  out of the plane of the ring for the radical.

One-dimensional B3LYP/6-311G(d,p) potential energy surfaces for the  $-C_2H_5$  torsional coordinates of the cation and radical are presented in Figure 5; all other internal coordinates are frozen at the minima shown in Figure 4. The potential energy surfaces reveal the presence of local minima for structures with

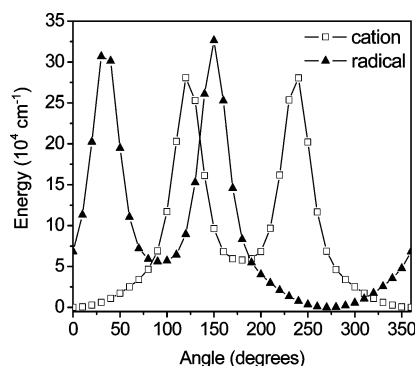


**Figure 5.** Potential energy surfaces for the torsional coordinate of the  $-C_2H_5$  group with respect to the plane of the aromatic ring computed at the B3LYP/6-311G(d,p) level. The global minima for the cation (open squares) and radical (filled triangles) have been shifted to zero. All other internal coordinates are frozen at the minima shown in Figure 4.

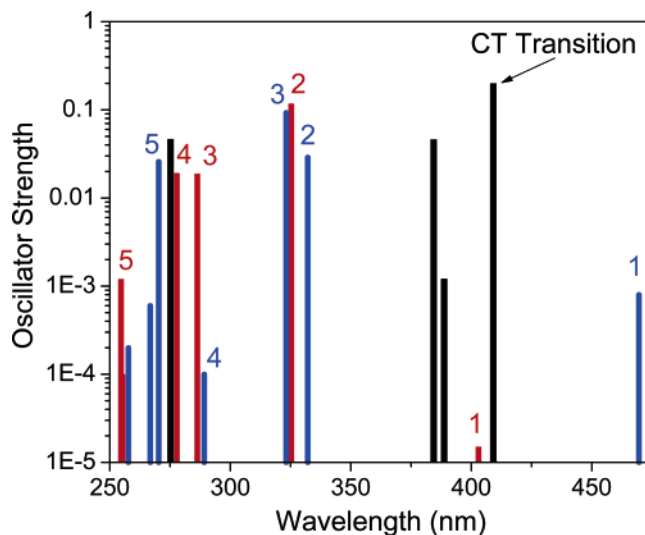


**Figure 6.** Linear absorption spectrum computed at the CIS/Lanl2DZ level for the ECMPI complex (black). Linear spectra for the radical (89 electrons) are computed with the CIS/6-311+G(d) method at the equilibrium geometry of the radical (red) and at the equilibrium geometry of the  $+1$  cation (blue). The lowest energy transition of ECMPI (black) at 409 nm has been assigned as the charge transfer (CT) transition, which is pumped in the experiment (see Figure 1). Transition indices for the radical correspond to those given in Table 1. (Note the logarithmic vertical scale.)

the  $-C_2H_5$  group oriented  $180^\circ$  from the global minima shown in Figure 4. These calculations suggest that the saturated hydrocarbon moiety,  $-C_2H_5$ , couples to the electronic structure of the aromatic ring to a degree that is not necessarily intuitive based on the conventions of molecular orbital theory. Empirical support for this interpretation is given by an experimental study of the infrared spectra of analogous compounds in which the vibrational frequency of the carbonyl group was found to be  $\sim 100\text{ cm}^{-1}$  greater for 1-ethyl-4-(carbomethoxy)pyridine than for methyl isonicotinate (same structure but without an ethyl group).<sup>34</sup>

Calculated linear spectra for ECMPI and the 1-ethyl-4-(carbomethoxy)pyridine radical are presented in Figure 6. The spectra of the radicals are computed at the equilibrium geometries of the cation (blue bars) and the radical (red bars). We assign the lowest energy transition of ECMPI (black bars) as the charge transfer excitation that is pumped in the experiment. This assignment is made on the basis of its oscillator strength and transition density, which is discussed in more detail below. The equilibrated radical (red bars) is an appropriate model for

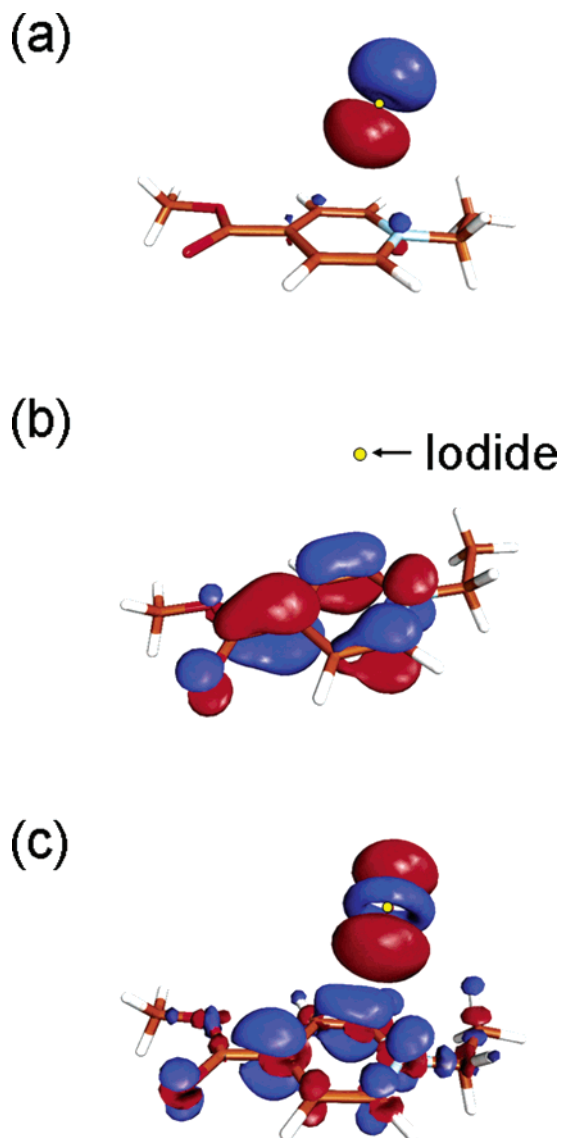


**Figure 7.** (a) HOMO for ECMPI at a contour level of 0.05 esu/bohr. (b) LUMO for ECMPI at a contour level of 0.05 esu/bohr. (c) Transition density of ECMPI at a contour level of 0.003 esu/bohr<sup>3</sup>. The red and blue surfaces represent positive and negative signs, respectively.

the system after relaxation has occurred in the excited state, whereas the radical at the equilibrium geometry of the cation (blue bars) represents the initially excited system at the nonequilibrium Franck–Condon geometry.

The highest occupied molecular orbital (HOMO) and lowest unoccupied molecular orbital (LUMO) for the ground electronic state of ECMPI are presented in Figure 7a and 7b, respectively. The HOMO is localized on the iodide ion, and the LUMO is localized on the cation. The lowest energy excitation of ECMPI (Figure 6) is characterized by a 38% HOMO-to-LUMO substitution in an expansion of singly excited configurations. The total real-space transition density for the charge transfer excitation of ECMPI is shown in Figure 7c. The transition involves a significant transfer of charge from the iodide ion to the 1-ethyl-4-(carbomethoxy)pyridinium cation, as indicated by the positive (blue) and negative (red) contour surfaces. The transitions calculated at 384 and 389 nm for the ECMPI complex (see Figure 6) possess similar transition densities to that shown in Figure 7c; charge is transferred from the p-orbitals of the iodide ion to the LUMO (Figure 7b). We take the excitation at 409 nm to be the best assignment for the experimentally pumped

**TABLE 1: Anisotropies Computed with Electronic Structure Calculations**

transition	wavelength/nm	osc str	$r(T)^a$
Ion Geometry			
1	470	0.0008	−0.16
2	332	0.0289	0.25
3	323	0.0929	0.23
4	289	0.0001	0.26
5	270	0.0259	0.29
Radical Geometry			
1	403	0.0000	−0.12
2	325	0.1174	−0.18
3	286	0.0188	0.20
4	278	0.0191	0.39
5	255	0.0001	0.30

<sup>a</sup> Equation 12.

charge transfer band because it is the lowest energy transition with the greatest oscillator strength. The transition dipole for the excitation at 384 nm, the other reasonable assignment for the charge transfer transition, differs from that at 409 nm by 2°. Therefore, the ambiguity in our assignment is virtually irrelevant with respect to computing pump–probe anisotropies.

The pump–probe anisotropies given in Table 1 are computed using the lowest energy transition for ECMPI (pumped) and the five lowest energy transitions of the radicals (probed) using

$$r(T = T') = \frac{3 \cos^2(\theta) - 1}{5} \quad (12)$$

where  $\theta$  is the angle between the charge transfer transition dipole and the transition dipole for the excitation of the radical. The indices used in Table 1 correspond to those given in Figure 6. The argument is written as  $T = T'$  because the angle may be dynamic in  $T$ . Bleach of the charge transfer band is neglected in eq 12 due to the dominant contribution of transient absorption of the radical to the experimental signals. In the simplest interpretation, the anisotropies calculated at the equilibrium geometry of the cation represent the  $T = 0$  pump–probe anisotropy, whereas the anisotropies computed at the equilibrium geometry of the radical correspond to the anisotropy after relaxation of the photoexcited state. Qualitatively, these calculations predict that the higher energy transitions have transition dipole orientations that are most similar to that of the charge transfer excitation, states for which  $r(T) = 0.2$ – $0.3$  in Table 1. The transition dipoles of the radical are dominated by components in the plane of the aromatic ring for both the equilibrium geometries of the cation and the radical. As seen in Figure 7, the charge transfer excitation also possesses a significant in-plane component that is nearly orthogonal to the N(1)–C(4) axis of the ring. Thus, the lowest energy transitions (transitions 1 and 2 for the radical geometry and transition 1 for the ion geometry, see Table 1), which give the smallest anisotropies, exhibit transition dipoles that are roughly oriented along the N(1)–C(4) axis of the ring.

**B. Pump–Probe.** The  $S_{zzzz}(T)$  pump–probe data presented in Figure 8 were recorded with the high-rep-rate, low-dispersion laser system, which has a 60 fs (Gaussian fwhm) instrument response function.<sup>68</sup> Figure 8a shows how the signal originating from the solvent is subtracted to give a corrected pump–probe

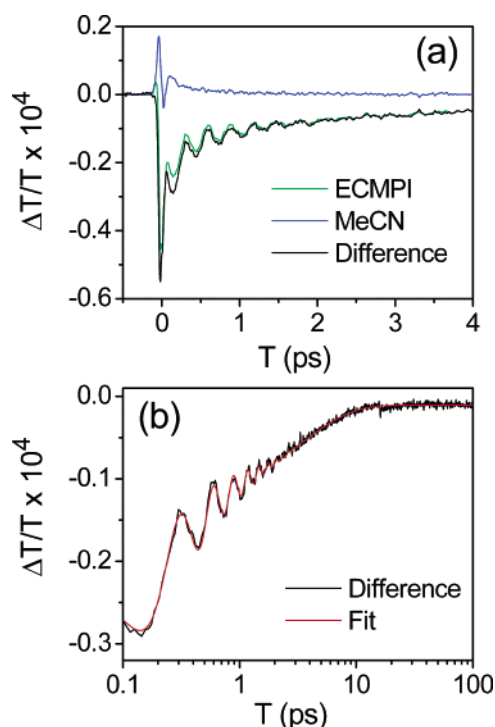


**Figure 8.** (a)  $S_{zzzz}(T)$  pump-probe signals, eq 7, for pure MeCN (blue) and a 0.3 OD solution of ECMPI (green). The black line is the difference ECMPI-MeCN. (b) A nonlinear least-squares fit (red) to the corrected pump-probe signal (black) using eq 13.

**TABLE 2: Nonlinear Least-Squares Fit to the  $S_{zzzz}(T)$  Pump-Probe Data Presented in Figure 8**

parameter <sup>a</sup>	value <sup>b</sup>
$a_1$	-0.106
$a_2$	-1.90
$a_3$	-1.25
$a_4$	0.600
$\alpha_1$	$\infty$
$\alpha_2$	0.26 ps
$\alpha_3$	3.4 ps
$\alpha_4$	0.71 ps
$\omega$	115 cm <sup>-1</sup>
$\Phi$	-23.9°

<sup>a</sup> Parameters are defined in eq 13. <sup>b</sup> The  $a_i$  coefficients have the units of  $10^5 \Delta T/T$ .

profile. The corrected data set is plotted on a log scale in Figure 8b along with a nonlinear least-squares fit to the function

$$F(T) = \sum_{i=1}^3 a_i \exp(-T/\alpha_i) + a_4 \exp(-T/\alpha_4) \cos(\omega T + \Phi) \quad (13)$$

The analysis is performed over the time range from  $T = 0.1$  to 100 ps (the spike at  $T = 0$  is not included). The resulting parameters presented in Table 2 indicate relaxation dynamics on several time scales. The  $\alpha_1$  time constant probably represents the creation of 1-ethyl-4-(carbomethoxy)pyridinium radicals that do not relax electronically within the 100 ps time window of the experiment. The fitting parameters suggest that  $\sim 4\%$  of the excited ion pairs become stable solvated radicals. The creation of stable radicals should be most facile in complexes that are loosely bound and able to separate following excitation.<sup>70–72</sup> This process is depicted in Figure 9 as evolution from the solvent-separated to the solvated radical solute-solvent configuration. The creation of solvated radicals is a reasonable interpretation, given the high stability of 1-ethyl-4-(carbomethoxy)-

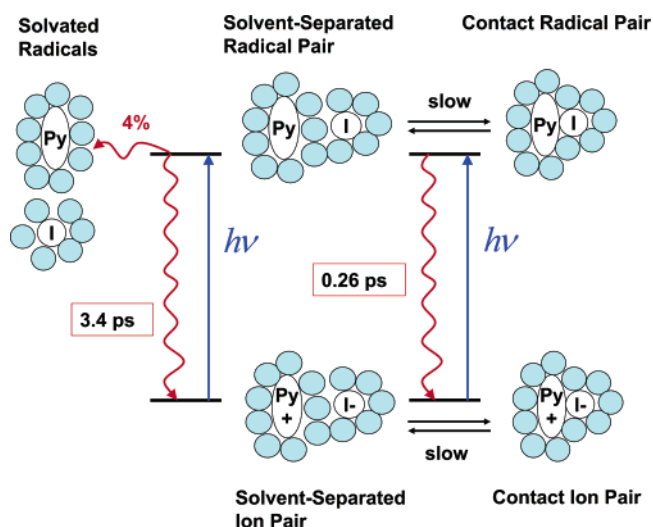


**Figure 9.** Cartoon representing the three solute-solvent configurations associated with components of the fit displayed in Figure 8. Photoinduced electron transfer occurs in both contact ion pairs and solvent-separated ion pairs, which subsequently relax with time constants of  $\alpha_2 = 0.26$  ps and  $\alpha_3 = 3.4$  ps, respectively. A fraction ( $\sim 4\%$ ) of all species excited in the experiment of the solvent-separated radical pairs become stable solvated radicals and do not relax to reform ion pairs, i.e.,  $\alpha_1 = \infty$  ps.

pyridine in solution.<sup>34,39</sup> However, we cannot rule out the possibility that the first term in eq 13 represents the creation of a photoproduct that is distinct from solvated iodine and 1-ethyl-4-(carbomethoxy)pyridinium radicals.

The second and third terms in eq 13 describe two finite electronic relaxation processes. As these time constants,  $\alpha_2$  and  $\alpha_3$ , differ by an order of magnitude, it is likely that they represent distinct ion pair configurations that differ primarily in the distance between the donor and acceptor.<sup>33,73</sup> In the context of a traditional model for solvated ion pairs, the  $\alpha_3$  time constant may be associated with relaxation of the solvent-separated radical pairs pictured in Figure 9, whereas contact radical pairs give rise to the  $\alpha_2$  decay time.<sup>38</sup> This interpretation assumes that the laser beam, which is tuned near the charge transfer peak maximum (Figure 1), is capable of exciting both the contact and solvent-separated ion pairs. Although the solvent-separated ion pairs probably absorb at higher frequencies than the contact ion pairs,<sup>72,74</sup> these inhomogeneous bands may overlap such that it is possible to excite both configurations with a pulse tuned to an intermediate frequency.<sup>31</sup> The solvent-separated ion pair is expected to possess a smaller charge transfer absorption cross section than the contact ion pair.<sup>72,74</sup> Therefore, the similar magnitudes of the  $a_2$  and  $a_3$  coefficients suggest that the equilibrium population of the solvent-separated ion pair is greater than that of the contact ion pair at 400 nm.

To summarize, we propose that the exponential decay constants for the first three terms in eq 13,  $\alpha_1$ – $\alpha_3$ , represent the three solute-solvent configurations illustrated in the kinetic scheme in Figure 9. The fourth term,  $\alpha_4$ , corresponds to a vibrational mode and is not explicitly linked to a specific solute-solvent configuration. We have evoked this traditional model for charge transfer in solvated ion pairs to clearly communicate our general conclusion that the decay time constants are associated with distinct solute-solvent configurations that are primarily defined by the donor-acceptor distance.<sup>38</sup> However, it should be acknowledged that the intermolecular orientation of the donor and acceptor may also contribute to the observed decay components. The failure of self-consistent field convergence with first principles basis sets precludes



quantitative presentation of an alternative to the geometry pictured in Figure 4a.

The dependence of the electron transfer rate on the donor–acceptor (DA) separation is described by  $k(r) = k(r_0) \exp[-\beta(r - r_0)]$ , where  $k(r_0)$  contains the Franck–Condon information,  $r_0$  is the DA separation of the contact ion pair,  $r$  is the DA separation for an arbitrary solvated ion pair configuration, and  $\beta$  describes the distance dependence of the electronic relaxation rate.<sup>75</sup> To estimate the donor–acceptor (DA) separation for the solvent-separated ion pair, we parametrize this formula with the measured time constant ( $1/k(r_0) = 0.26$  ps) and calculated separation ( $r_0 = 0.37$  nm, see Figure 4a) of the contact ion pair. Given a typical value of  $\beta$  for long-range electron transfer,  $\beta = 1.2 \text{ \AA}^{-1}$ ,<sup>75–78</sup> the DA separation for the solvent-separated ion pair is  $r = 4.8 \text{ \AA}$ . This value is not consistent with the scheme presented in Figure 9, where it is assumed that both complexes are photoexcited in similar populations, because a  $1.1 \text{ \AA}$  difference in the DA separation for the two complexes should give rise to vastly different oscillator strengths and excited state populations.<sup>72,74</sup> It was recently suggested that the effective  $\beta$  value for DA pairs in close contact (i.e.,  $\sim 0.5 \text{ \AA}$ ) is on the order of  $\beta = 4 \text{ \AA nm}^{-1}$ .<sup>79</sup> The calculated DA separation for the solvent-separated ion pair is  $r = 4.0 \text{ \AA}$  with  $\beta = 4 \text{ \AA}^{-1}$ , which is more consistent with our interpretation.

The present analysis of the relationship between the electronic relaxation rate and the DA separation confronts a fundamental assumption of Figure 9: the interconversion of contact and solvent-separated ion pairs is slow compared to the 3.4 ps electronic relaxation rate of the latter. Indeed, an alternative scheme can be proposed in which the contact ion pair possesses a much greater oscillator strength than the solvent-separated ion pair complex and is therefore the only species populated at  $T = 0$ . In this scenario, the slower relaxation parameter,  $\alpha_3$ , would be associated with reorganization of the radical pair/solvent configuration, that is, electron transfer adiabaticity.<sup>80–85</sup> Although adiabaticity effects cannot be ruled out with the present experiments, we will assume that the ion pair configurations do not interconvert on the 3.4 ps time scale.

The periodic modulation of the pump–probe signal is described by the fourth term in eq 13. This term has an oscillation frequency of  $115 \text{ cm}^{-1}$  ( $\omega$ ), a damping time of 710 fs ( $\alpha_4$ ), and an amplitude ( $a_4$ ) that is comparable to the total signal strength. This vibration, which was previously observed in a surface enhanced Raman scattering study,<sup>86</sup> cannot be unambiguously assigned with the present information. However, the best candidates may be considered on the basis of a normal-mode analysis for the radical at the B3LYP/6-311G(d,p) level. Torsional modes, with respect to the plane of the ring, of the ethyl and ester groups are computed at 54 and  $94 \text{ cm}^{-1}$ , respectively. As discussed above, the  $-\text{C}_2\text{H}_5$  group is significantly displaced along this coordinate upon one electron reduction. However, the main problem with this assignment is that torsional modes are not expected to be underdamped due to associated solvent displacement. The underdamped character of the vibration means that it does not couple strongly to the surrounding solvent and is probably dominated by motion in the plane of the ring. A bending mode of the ester group calculated at  $139 \text{ cm}^{-1}$  fits this criterion. The pyramidalization mode of the amino group computed at  $175 \text{ cm}^{-1}$  is another possibility. The latter is likely to be lower in frequency in solution than in vacuo.

The intermolecular donor–acceptor Coulomb force is certain to be affected by the charge transfer excitation. Therefore,

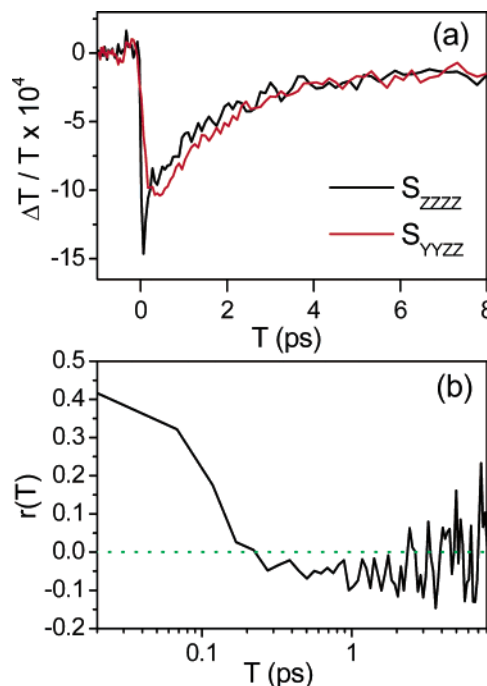


**Figure 10.** (a)  $S_{ZZZZ}(T)$  and  $S_{YYZZ}(T)$  pump–probe signals for ECMPI are given by the black and red lines, respectively. (b) The pump–probe anisotropy (solid black line), eq 8, calculated using the data in panel a. The dotted green line is  $r(T) = 0$ .

modulation of the donor–acceptor distance should also be considered as the identity of the mode that gives rise to the oscillatory component of the pump–probe signal. The fact that a  $112 \text{ cm}^{-1}$  recurrence is observed in pump–probe experiments on the B state of molecular iodine lends strong support to this possibility.<sup>87,88</sup> This assignment requires that the motion along the intermolecular coordinate is underdamped and it does involve significant solvent displacement. Scherer et al.'s pump–probe study of solvated molecular iodine yielded a 220 fs damping constant for this vibration, which suggests that underdamped motion of iodine along this charge transfer coordinate is a reasonable conjecture.<sup>88</sup>

$S_{ZZZZ}(T)$  and  $S_{YYZZ}(T)$  pump–probe signals and the corresponding anisotropy (see eq 8) are presented in Figure 10. These data were collected with the 1 kHz laser system described above, which has a 125 fs instrument response function and is somewhat noisier than the high-rep-rate system used to obtain the data shown in Figure 8. The nuclear coherence is not observed due to these factors. The  $S_{ZZZZ}(T)$  and  $S_{YYZZ}(T)$  profiles are similar in magnitude and shape, although significant deviation is found for delay times less than 1 ps. The  $S_{ZZZZ}(T)$  signal exhibits a narrow feature near  $T = 0$  similar to that observed in Figure 8, whereas the  $S_{YYZZ}(T)$  signal rises more slowly. The anisotropy,  $r(T)$ , shown in Figure 10b has an initial value of 0.4, and it decays to  $-0.05$  within 500 fs. Assuming transient absorption of the radical dominates the pump–probe signals, the angle between the transition dipoles of the pumped and probed transitions is  $\sim 60^\circ$  for  $T > 1$  ps (eq 12). Similar anisotropy decays have been observed for systems of electronically coupled chromophores.<sup>46,89–94</sup> However, ECMPI is not an excitonic system and the absorption spectrum of its radical does not indicate the presence of multiple transitions in the 400 nm region.<sup>34</sup> This leads us to conclude that nuclear relaxation is the origin of the sub-picosecond change in the anisotropy.

It should be noted that the rotational diffusion time of ECMPI in acetonitrile is expected to be long compared to the electronic relaxation process. The rotational diffusion time may be



computed using the Stokes–Einstein–Debye relation,<sup>95</sup>  $t_r = V\eta/k_B T$ , where  $\eta$  is the viscosity of acetonitrile at 300 K (0.35 cP).<sup>96</sup> Assuming a spherical shape, the volume inside a contour of 0.001 esu/bohr<sup>3</sup> for ECMPI is 0.52 nm<sup>3</sup>, as computed using the volume keyword at the B3LYP/Lanl2DZ level<sup>65</sup> with the geometry given in Figure 4a. These parameters yield  $t_r = 44$  ps. Therefore, rotation of the solute may be neglected in the interpretation of the pump–probe anisotropy.

Our calculations and a previous experimental study of vibrational spectra of analogous compounds<sup>34</sup> (see section VA) suggest that the orientation of the  $-\text{C}_2\text{H}_5$  group is strongly coupled to the electronic structure of the acceptor and is therefore likely to be associated with the sub-picosecond anisotropy decay. However, the calculated anisotropies in Table 1 do not lend direct support to this interpretation due to the ambiguity in assigning the transition that is experimentally probed. As discussed above, the best approximation to the  $T = 0$  and asymptotic values of the anisotropy are given by calculations for the radical at the equilibrium geometries of the cation and radical, respectively. The assignment of the probed transition to excitation 2 or 3 at the geometry of the ion is most consistent with the observed anisotropy at  $T = 0$  ps. Furthermore, the assignment of transition 2 at the geometry of the radical is most consistent with the experimental anisotropy for  $T > 1$  ps. These assignments assume that the computed transition frequencies are overestimated, which is reasonable considering that the calculations are performed in vacuo. Solvent effects may also explain the differences of 0.1–0.2 in the calculated and measured values of the anisotropy. These calculations support the interpretation that overdamped relaxation along the  $-\text{C}_2\text{H}_5$  torsional coordinate following charge transfer and the associated electronic relaxation is the origin of the sub-picosecond decay in the anisotropy.

**C. Electric-Field-Resolved Transient Grating.** The amplitudes of the EFR-TG signals for pure MeCN and the ECMPI solution are presented in Figure 11. Comparison of parts a and b of Figure 11 suggests that the solvent contribution to the signal is dominant when the pulses are overlapped in the ECMPI solution due to the strong electronic nonlinearity of the solvent.<sup>47</sup> The amplitude of the EFR-TG signal for ECMPI decays with similar dynamics to the pump–probe profiles for delay times large enough ( $T > 300$  fs) that signal emission from the solvent is negligible. This similarity is expected, as the transient grating and the pump–probe techniques are both designed to interrogate dynamics in  $T$ .<sup>56</sup>

The spectral phases of the EFR-TG signals,  $\varphi_s(\omega_t)$ , for pure MeCN are shown in Figure 12a. Inspection of the phase surface reveals that the linear spectral phase (i.e., the slope of the phase with respect to  $\omega_t$ ) is positive for negative  $T$  and negative for positive  $T$ . The linear spectral phase represents the group delay of the signal pulse. Thus, the signal is emitted before and after the peak of the probe pulse arrives at the sample for positive and negative  $T$ , respectively. In the approximation that MeCN responds instantaneously to the field of the laser pulses, the signal emission time is determined solely by the convolution of the 1–2 pulse pair with pulse 3. The approximation of instantaneous response amounts to ascribing signal emission of MeCN to its electronic nonlinearity and neglecting the nuclear response. We have found that the nuclear response gives rise to asymmetry of the signal emission time with respect to  $T = 0$ .<sup>97</sup> In general, solvents with the strongest nuclear responses possess the most asymmetric emission times.

The phase surface for ECMPI shown in Figure 12b is similar to that of MeCN for negative  $T$  but differs for positive  $T$ .

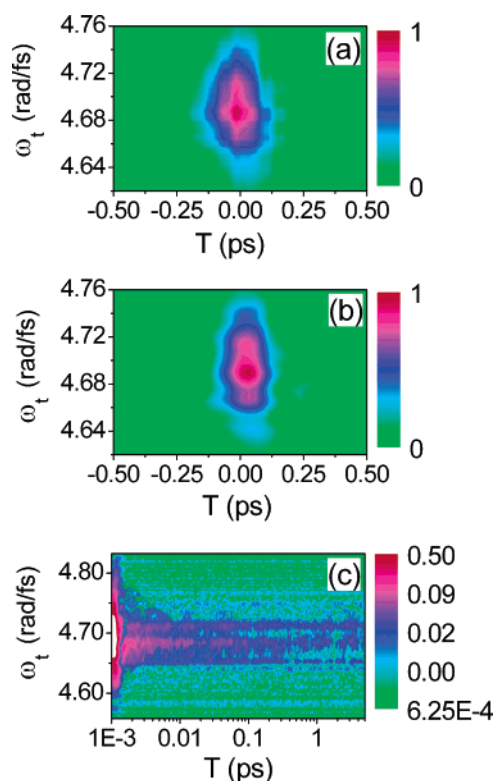


**Figure 11.** Absolute value of the experimental EFR-TG signals, eq 11, for (a) pure MeCN and (b and c) ECMPI. Panels b and c contain the same data. The signal is plotted on a linear scale in panels a and b. The log of the signal is plotted in panel c.

Specifically, the linear spectral phase for ECMPI is less negative than that of MeCN for positive  $T$ ; this difference originates from the picosecond relaxation time scale of the population grating for ECMPI versus the electronic polarizability response of MeCN, which relaxes on the femtosecond time scale.<sup>47,98</sup> The linear spectral phase for ECMPI converges to zero for delays greater than 300 fs when signal emission by the solvent has become negligible. This behavior is consistent with theoretically simulated EFR-TG signals for resonant systems using realistic response functions and finite laser pulses.<sup>46</sup> These data (Figure 12) completely represent the additional information obtained by spectral interferometry with respect to conventional measurements. The signal phase is not fully obtained by pump–probe, homodyned transient grating, or recent implementations of heterodyned transient grating with wavelength-integrated detection.<sup>42,45</sup>

One-dimensional slices of the phase surfaces are presented in Figure 13. The data are plotted for three slices in  $\omega_t$ : 4.69, 4.73, and 4.66 rad/fs, which correspond to the signal peak maximum and the two frequencies that define the full width at half-maximum, respectively. The data for pure MeCN display the change in the sign of the slope of the spectral phase that occurs for positive and negative  $T$ . The linear spectral phase for the ECMPI solution is initially positive for negative  $T$ , similar to pure MeCN. However, the spectral phase has a significant quadratic contribution (the phase at 4.69 rad is greatest) between  $T = 0$  and  $T = 0.3$  ps. Our calculations of EFR-TG signal fields for electronically resonant solutes do not predict this amount of quadratic spectral phase.<sup>46</sup> It is possible that interference between signals emitted by the solute and solvent gives rise to an unanticipated effect in this delay range, where these signals are similar in magnitude.<sup>47</sup> Figure 13c shows that the linear spectral phase for the ECMPI solution converges to zero by  $T = 0.3$  ps and then continues to evolve for greater

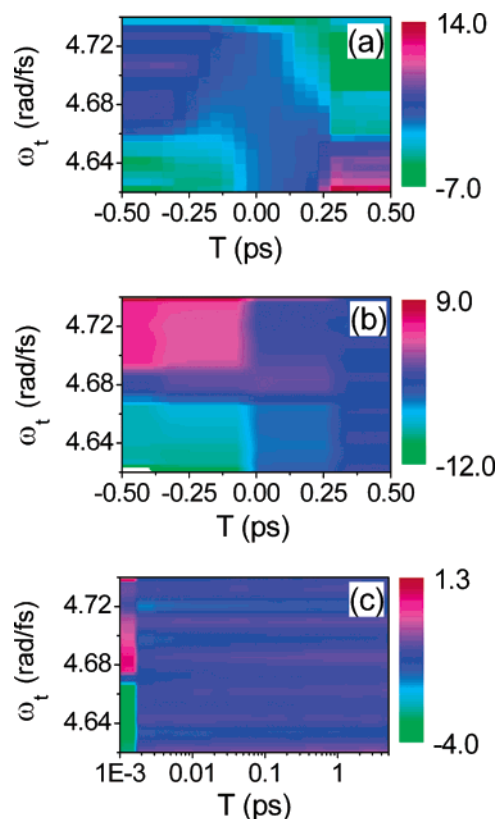


**Figure 12.** Phase of the experimental EFR-TG,  $\varphi_s(\omega_t)$  in eq 11, for (a) neat acetonitrile and (b and c) ECMPI. The pump–probe delay is plotted on a log scale in panel c. Together, these two-dimensional phase surfaces and the amplitudes given in the respective panels of Figure 11 completely represent the EFR-TG signal fields.

delay times with similar dynamics to those observed in the pump–probe measurements. The phase does not degenerate into noise at long delays,  $T$ , due to creation of the solvated free radicals associated with the first term in eq 13. The asymptotic value of the phase ( $\varphi_s \approx -1.0$  rad) is determined by the electronic resonance spectrum of the solvated free radical. Therefore, the fact that  $\varphi_s$  evolves after  $T > 300$  fs suggests that the electronic resonance spectra of the contact and solvent-separated radicals pairs ( $\varphi_s \approx -1.25$  rad) is slightly different than that of the solvated free radicals ( $\varphi_s \approx -1.0$  rad). The observation of similar dynamics in the pump–probe profile and EFR-TG signal phases provides additional information on the photochemistry of ECMPI.

## VI. Discussion

The electronic relaxation dynamics of the photoinduced charge transfer state are obtained from the pump–probe measurement. However, the pump–probe measurement does not necessarily rule out alternatives to the mechanisms presented in Figure 9, particularly if they are associated with species that absorb in regions outside the laser pulse spectrum. As discussed in section II, the signal phase is sensitive to dynamics occurring at frequencies outside the laser pulse spectrum by way of the Kramers–Kronig relation between the real and imaginary components of the signal.<sup>42,51–53</sup> Below, we suggest a plausible mechanism that is not represented in Figure 9 to illustrate the sensitivity of the EFR-TG signal phase to a chemical process that the pump–probe and EFR-TG signal amplitudes are unable to detect.

It has been suggested that MeCN reacts with solvated electrons to form a radical anion that absorbs strongly in the

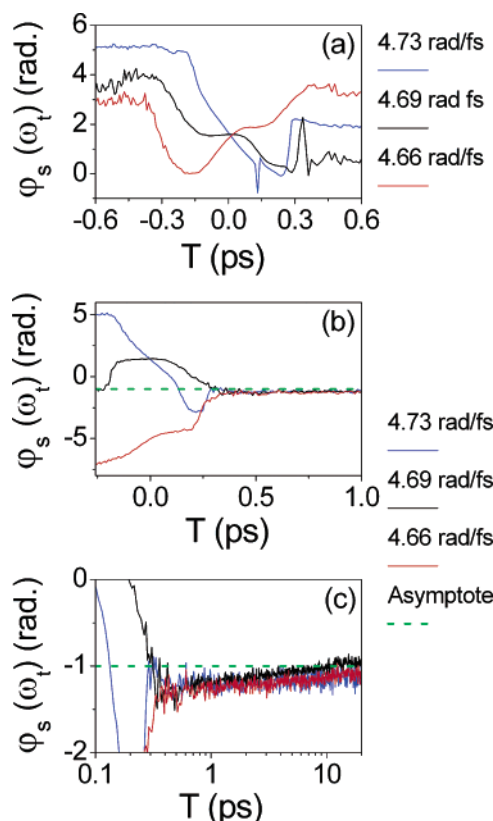


**Figure 13.** Phase of the experimental EFR-TG,  $\varphi_s(\omega_t)$  in eq 11, for (a) neat acetonitrile and (b and c) ECMPI. These data are slices in  $\omega_t$  of the two-dimensional phase surfaces presented in Figure 12. The value of  $\omega_t$  is given in the figure legend.

near infrared with an absorption maximum at 1400 nm ( $\epsilon \approx 23\,000\text{ M}^{-1}\text{ cm}^{-1}$ ).<sup>99</sup> This near-infrared absorption band was observed in recent femtosecond pump–probe measurements and reinterpreted as arising from solvated electrons.<sup>100</sup> Xia et al.’s argument for the existence of solvated electrons is supported by electron scavenging experiments, quantum chemical calculations, and comparison to an indole–acetonitrile system. To illustrate the unique information content of the EFR-TG signal phase, we will consider the sensitivity of EFR-TG to the existence of this species, which we take to be a solvated electron for simplicity.

The information content of the EFR-TG signal phase may be illustrated qualitatively by assuming delta function laser pulses. In this limit, the transient grating signal has a simple interpretation. The absorptive component is given by the instantaneous extinction coefficient of the photoexcited species, which generally evolves in the delay,  $T$ , due to electronic and nuclear relaxation. The dispersive part of the signal is obtained by the Kramers–Kronig transform of the absorptive part multiplied by  $-1$ . This model was presented in ref 101 and used to interpret the spectral dependence of wavelength-integrated heterodyned transient grating measurements. We prefer this approximate approach to a full calculation of the signal for a three-level system with finite laser pulses because the model is intuitive and reasonably accurate.

The relation between the EFR-TG signal field and the third-order polarization is given in eq 6. In the impulsive limit, the dispersive part of the polarization is related to the absorptive part by the Kramers–Kronig transform

$$\text{Re}\{P^{(3)}(\omega_i, T)\} = \frac{-1}{\pi} \mathcal{P} \int_{-\infty}^{\infty} d\omega'_i \frac{\text{Im}\{P^{(3)}(\omega'_i, T)\}}{\omega'_i - \omega_i} \quad (14)$$

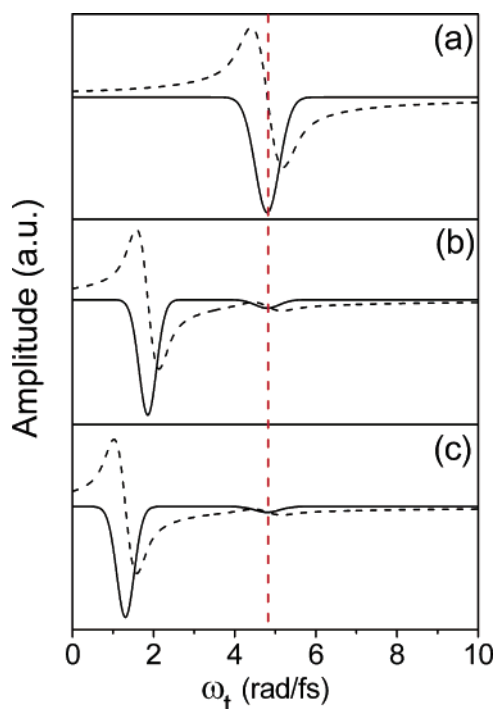


**Figure 14.** Real (solid) and imaginary (dashed) parts of  $P^{(3)}(\omega_t, T)$ . The imaginary part is given by eq 16, and the real part is computed with eq 14. The resonances are located at (a) 4.82 rad/fs, (b) 4.82 and 1.34 rad/fs, and (c) 4.82 and 1.88 rad/fs. The extinction coefficients for the lower energy resonances in panels b and c are 5.35 times greater than that of the transition at 4.82 rad/fs. The dotted red line marks  $\omega_t = 4.82$  rad/fs.

where  $\mathcal{P}$  stands for the principal part. Equation 14 assumes delta function laser pulses.  $\text{Re}\{P^{(3)}(\omega_t, T)\}$  is generally dynamic in  $T$  due to electronic and nuclear relaxation. In terms of the polarization, the signal phase is defined by

$$\varphi(\omega_t, T) = -\arctan \left[ \frac{\text{Re}\{P^{(3)}(\omega_t, T)\}}{\text{Im}\{P^{(3)}(\omega_t, T)\}} \right] \quad (15)$$

The absorptive component of  $P^{(3)}(\omega_t, T)$  is proportional to the extinction coefficient of the probed transition(s) at the delay time,  $T$ , that is,

$$\text{Im}\{P^{(3)}(\omega_t, T)\} \propto \frac{\epsilon_{\text{pr}}(\omega_t, T)}{\omega_t} \quad (16)$$

$\text{Im}\{P^{(3)}(\omega_t, T)\}$  is negative for transient absorption under this paper's convention (see section IIC). Calculation of the signal phase requires knowledge of the ratio of the real and imaginary parts of  $P^{(3)}(\omega_t, T)$ . Therefore, constant coefficients may be neglected and the signal phase for the present model may be written as

$$\varphi(\omega_t, T) = -\arctan \left[ \frac{\omega_t \eta(\omega_t, T)}{\epsilon_{\text{pr}}(\omega_t, T)} \right] \quad (17)$$

where

$$\eta(\omega_t, T) = \frac{-1}{\pi} \mathcal{P} \int_{-\infty}^{\infty} d\omega'_t \frac{\epsilon_{\text{pr}}(\omega'_t, T)}{\omega'_t(\omega'_t - \omega_t)} \quad (18)$$

The real and imaginary parts of  $P^{(3)}(\omega_t, T)$  are shown in Figure 14 for three separate cases. The first system in Figure 14a

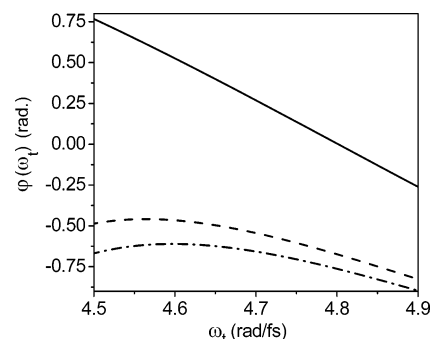


**Figure 15.** Signal phases computed with eq 18. The solid, dashed, and dashed-dotted lines correspond to panels a, b, and c in Figure 14. The solid line possesses single transient resonance at 4.82 rad/fs and corresponds to the scheme given in Figure 9. Parts b and c of Figure 14 represent a scenario in which photoexcitation of the ion pair creates both the radical (4.82 rad/fs) and a solvated electron that absorbs at 1.88 and 1.34 rad/fs, respectively.<sup>99,100</sup> These two spectra are taken to represent separate snapshots of the solvation process in  $T$ . The ratio of the extinction coefficients for the solvated electron and radical,  $\epsilon_{\text{pr}}(\omega_t, T)$ , is set to 5.3;<sup>34,99</sup> the model assumes that the two species are created with equal probabilities.

The goal of this calculation is to compute the effect of spectral evolution of the solvated electron (i.e., solvation) on the signal phase in the region of the experimental laser pulse spectrum. The EFR-TG signal phases for the three polarizations are given in Figure 15. The phase for the system with a single resonance (solid line) represents the scheme present in Figure 9; the absolute phase may differ from the observation due to the presence of additional strong resonances of the radical in the ultraviolet.<sup>34</sup> Figure 15 shows that spectral evolution of the solvated electron in the near-infrared results in a phase change of  $\sim 0.13$  rad at 4.64 rad/fs. Thus, EFR-TG is capable of sensing solvation dynamics in the 1000–1400 nm region with the present 405 nm degenerate pulse configuration. In this sense, EFR-TG measurements with our degenerate 90 fs pulses give similar information to that obtained in a pump–probe experiment with a hole-burning pulse configuration, which would involve replacing the probe pulse with a broadband continuum pulse.

## VII. Conclusion

Various aspects of the photophysics of ECMPI are investigated with this study of the polarization and phase dependence of its four-wave mixing signals. Pump–probe measurements reveal the presence of an underdamped vibrational mode with a frequency of  $115 \text{ cm}^{-1}$ , which is coupled to the photoinduced charge transfer transition (Figure 8). A high-level normal-mode analysis for the acceptor yields a bending mode of the ester group and a pyramidalization mode of the amino group near the frequency of the observed oscillation. It is also possible that this recurrence represents modulation of the intermolecular donor–acceptor distance. The underdamped  $112 \text{ cm}^{-1}$  vibration observed in pump–probe studies of solvated molecular iodine gives strong support to this assignment.<sup>88</sup> Electronic structure calculations (Figure 6) and previous infrared absorption studies with analogous compounds<sup>34</sup> suggest that the orientation of the  $-\text{C}_2\text{H}_5$  group is strongly coupled to the electronic structure of the 1-ethyl-4-(carbomethoxy)pyridine radical. These data lead us to conclude that reorientation of the  $-\text{C}_2\text{H}_5$  group underlies the observed sub-picosecond relaxation of the pump–probe anisotropy from  $r(T) = 0.4$  at  $T = 0$  ps to  $r(T) = -0.5$  for  $T > 1$  ps.



The present EFR-TG experiments and model calculations demonstrate that greater insight into photophysical processes may be obtained when the complete electric field, including the phase of the signal, is resolved. EFR-TG signals for pure MeCN show that the linear spectral phase (i.e., signal emission time) roughly follows the convolution of the pump and probe pulses (Figure 12). In contrast, this optical gating effect subsides for ECMP1 at positive delay times,  $T$ , and the spectral phase is determined by the line shape of its transient electronic resonance structure. Our model calculations demonstrate how the spectral phase is sensitive to resonances that exist outside the bandwidth of the probe pulses. The observed EFR-TG signal phases suggest that photoexcitation of the ion pair does not create species with strong resonances in the visible and near-infrared regions of the spectrum. Thus, the observed dynamics in the EFR-TG signal phase further supports the scheme presented in Figure 9.

**Acknowledgment.** This research was supported by the National Science Foundation (CHE 0317009 and NIRT ERC 0303389). We acknowledge Rene A. Nome and Jeongho Kim for their roles in developing the 1 kHz and high-rep-rate laser systems used in this work.

## References and Notes

- (1) Marcus, R. A.; Sutin, N. *Biochim. Biophys. Acta* **1985**, *85*, 811.
- (2) Barbara, P. F.; Meyer, T. J.; Ratner, M. A. *J. Phys. Chem.* **1996**, *100*, 13148.
- (3) Bixon, M.; Jortner, J. *Advances in Chemical Physics*; John Wiley and Sons: New York, 1999; Vol. 106.
- (4) Newton, M. D. *Electron Transfer in Chemistry*; Wiley-VCH: Weinheim, Germany, 2001.
- (5) Brunschwig, B. S.; Creutz, C.; Sutin, N. *Chem. Soc. Rev.* **2002**, *31*, 168.
- (6) Endicott, J. F.; Chen, Y. J.; Xie, P. *Coord. Chem. Rev.* **2005**, *249*, 343.
- (7) Guisinger, N. P.; Yoder, N. L.; Hersam, M. C. *Proc. Natl. Acad. Sci.* **2005**, *102*, 8838.
- (8) Friedman, R. S.; McAlpine, M. C.; Ricketts, D. S.; Ham, D.; Lieber, C. M. *Nature* **2005**, *434*, 1085.
- (9) Reed, M. A.; Lee, T., Eds. *Molecular Nanoelectronics*; American Scientific Publishers: 2003.
- (10) Joachim, C.; Ratner, M. A. *Proc. Natl. Acad. Sci. U.S.A.* **2005**, *102*, 8800.
- (11) Segal, D.; Nitzan, A.; Hanggi, P. *J. Chem. Phys.* **2003**, *119*, 6840.
- (12) Lee, C. H.; Yu, G.; Moses, D.; Heeger, A. J. *Synth. Met.* **1995**, *69*, 429.
- (13) Sheats, J. R.; Antoniadis, H.; Hueschen, M.; Leonard, W.; J. M.; Moon, R.; Roitman, D.; Stocking, A. *Science* **1996**, *273*, 5277.
- (14) Keir, P. D.; Wager, J. F. *Annu. Rev. Mater. Sci.* **1997**, *27*, 223.
- (15) Friend, R. H.; Gymer, R. W.; Holmes, A. B.; Burroughes, J. H.; Marks, R. N.; Taliani, C.; Bradley, D. D. C.; dos Santos, D. A.; Brédas, J. L.; Loglund, M.; Salaneck, W. R. *Nature* **1999**, *397*, 121.
- (16) Beljonne, D.; Pourtois, G.; Silva, C.; Hennebicq, E.; Herz, L. M.; Friend, R. H.; Scholes, G. D.; Setayesh, S.; Mullen, K.; Bredas, J. L. *Proc. Natl. Acad. Sci. U.S.A.* **2002**, *99*, 10982.
- (17) Fleming, G. R.; van Grondelle, R. *Curr. Opin. Struct. Biol.* **1997**, *7*, 738.
- (18) Sundstrom, V.; Pullertis, T.; van Grondelle, R. *J. Phys. Chem. B* **1999**, *103*, 2327.
- (19) Blankenship, R. E. *Molecular Mechanisms of Photosynthesis*; Blackwell Science: Oxford, U.K., 2002.
- (20) Schoenlein, R. W.; Peteanu, R. A.; Mathies, C. V. *Science* **1991**, *92*, 4012.
- (21) Wang, J. P.; El-Sayed, M. A. *Biophys. J.* **2001**, *80*, 961.
- (22) Ruhman, S.; Hou, B.; Friedman, N.; Ottolenghi, M.; Sheves, M. *J. Am. Chem. Soc.* **2002**, *124*, 8854.
- (23) Ulstrup, J.; Jortner, J. *J. Chem. Phys.* **1975**, *63*, 4358.
- (24) Jortner, J. *J. Chem. Phys.* **1976**, *64*, 4860.
- (25) Bixon, M. *Chem. Phys.* **1976**, *13*, 447.
- (26) Blackburn, R. L.; Johnson, C. S.; Hupp, J. T.; Bryant, M. A.; Sobocinski, R. L.; Pemberton, J. E. *J. Phys. Chem.* **1991**, *95*, 10535.
- (27) Tominaga, K.; Kliner, D. A. V.; Johnson, A. E.; Levinger, N. E.; Barbara, P. F. *J. Chem. Phys.* **1993**, *98*, 1228.
- (28) Wynne, K.; Galli, C. Hochstrasser, R. M. *J. Chem. Phys.* **1994**, *100*, 4797.
- (29) Britt, B. M.; McHale, J. L.; Friedrich, D. M. *J. Phys. Chem.* **1995**, *99*, 6347.
- (30) Myers, A. B. *Chem. Rev.* **1996**, *96*, 911.
- (31) Marin, T. W.; Homoelle, B. J.; Spears, K. G. *J. Phys. Chem. A* **2002**, *106*, 1152.
- (32) Cave, R. J.; Baxter, D. V.; Goddard, W. A., III; Baldeschwieler, J. D. *J. Chem. Phys.* **1987**, *87*, 926.
- (33) Newton, M. D. *Chem. Rev.* **1991**, *91*, 767.
- (34) Kosower, E. M.; Poziomek, E. J. *J. Am. Chem. Soc.* **1964**, *86*, 5515.
- (35) Kosower, E. M.; Cotter, J. L. *J. Am. Chem. Soc.* **1964**, *86*, 5524.
- (36) Monk, P. M. S. *The Viologens: Physicochemical Properties, Synthesis and Applications of the Salts of 4,4'-Bipyridine*; John Wiley and Sons: New York, 1999.
- (37) Kestner, N. R.; Logan, J.; Jortner, J. *J. Phys. Chem.* **1974**, *78*, 2148.
- (38) Reichardt, C. *Solvents and Solvent Effects in Organic Chemistry*; VCH: New York, 1990.
- (39) Kosower, E. M. *J. Am. Chem. Soc.* **1958**, *80*, 3253.
- (40) Goodno, G. D.; Dadusc, G.; Miller, R. J. D. *J. Opt. Soc. Am. B* **1998**, *15*, 1791.
- (41) Cowan, M. L.; Ogilvie, J. P.; Miller, R. J. D. *Chem. Phys. Lett.* **2004**, *386*, 184.
- (42) Xu, Q. H.; Ma, Y. Z.; Fleming, G. R. *J. Phys. Chem. A* **2002**, *106*, 10755.
- (43) Brixner, T.; Mancal, T.; Stiopkin, I. V.; Fleming, G. R. *J. Chem. Phys.* **2004**, *121*, 4221.
- (44) Brixner, T.; Stenger, J.; Vaswani, H. M.; Cho, M.; Blankenship, R. E.; Fleming, G. R. *Nature* **2005**, *434*, 625.
- (45) Goodno, G. D.; Astinov, V.; Miller, R. J. D. *J. Phys. Chem. A* **1999**, *103*, 10360.
- (46) Moran, A. M.; Maddox, J. B.; Hong, J. W.; Kim, J.; Nome, R. A.; Bazan, G. C.; Mukamel, S.; Scherer, N. F. *J. Chem. Phys.* **2006**, *124*, 194904.
- (47) Moran, A. M.; Nome, R. A.; Scherer, N. F. *J. Chem. Phys.*, in press.
- (48) Brito-Cruz, C. H.; Fork, R. L.; Knox, W. H.; Shank, C. V. *Chem. Phys. Lett.* **1986**, *132*, 341.
- (49) Murakami, H.; Kinoshita, S.; Hirata, Y.; Okada, T.; Mataga, N. *J. Chem. Phys.* **1992**, *97*, 7881.
- (50) Ma, J.; Vanden Bout, D. A.; Berg, M. *J. Chem. Phys.* **1995**, *103*, 9146.
- (51) Nelson, K. A.; Casalegno, R.; Miller, R. J. D.; Fayer, M. D. *J. Chem. Phys.* **1982**, *77*, 1144.
- (52) Hybl, J. D.; Ferro, A. A.; Jonas, D. M. *J. Chem. Phys.* **2001**, *115*, 6606.
- (53) Hybl, J. D.; Yu, A.; Farrow, D. A.; Jonas, D. M. *J. Phys. Chem. A* **2002**, *106*, 7651.
- (54) Voronine, D.; Abramavicius, D.; Mukamel, S. *J. Chem. Phys.* **2006**, *124*, 034104.
- (55) Trebino, R. *Frequency Resolved Optical Gating: The Measurement of Ultrashort Laser Pulses*; Kluwer Academic Publishers: Boston, Dordrecht, The Netherlands, London, 2000.
- (56) Mukamel, S. *Principles of Nonlinear Optical Spectroscopy*; Oxford University Press: New York, Oxford, U.K., 1995.
- (57) Lepetit, L.; Chéiaux, G.; Joffre, M. *J. Opt. Soc. Am. B* **1995**, *12*, 2467.
- (58) Dorrer, C.; Belabas, N.; Likforman, J. P.; Joffre, M. *J. Opt. Soc. Am. B* **2000**, *17*, 1795.
- (59) Tokunaga, E.; Terasaki, A.; Kobayashi, T. *J. Opt. Soc. Am. B* **1995**, *12*, 753.
- (60) Gallagher, S. M.; Albrecht, A. W.; Hybl, J. D.; Landin, B. L.; Rajaram, B.; Jonas, D. M. *J. Opt. Soc. Am. B* **1998**, *15*, 2338.
- (61) Khalil, M.; Demirdoven, N.; Tokmakoff, A. *J. Phys. Chem. A* **2003**, *107*, 5258.
- (62) Belabas, N.; Jonas, D. M. *J. Opt. Soc. Am. B* **2005**, *22*, 655.
- (63) Brixner, T.; Stiopkin, I. V.; Fleming, G. R. *Opt. Lett.* **2004**, *29*, 884.
- (64) Jonas, D. M. *Annu. Rev. Phys. Chem.* **2003**, *54*, 425.
- (65) Frisch, M. J.; Trucks, G. W.; Schlegel, H. B.; Scuseria, G. E.; Robb, M. A.; Cheeseman, J. R.; Montgomery, J. A., Jr.; Vreven, T.; Kudin, K. N.; Burant, J. C.; Millam, J. M.; Iyengar, S. S.; Tomasi, J.; Barone, V.; Mennucci, B.; Cossi, M.; Scalmani, G.; Rega, N.; Petersson, G. A.; Nakatsuji, H.; Hada, M.; Ehara, M.; Toyota, K.; Fukuda, R.; Hasegawa, J.; Ishida, M.; Nakajima, T.; Honda, Y.; Kitao, O.; Nakai, H.; Klene, M.; Li, X.; Knox, J. E.; Hratchian, H. P.; Cross, J. B.; Bakken, V.; Adamo, C.; Jaramillo, J.; Gomperts, R.; Stratmann, R. E.; Yazyev, O.; Austin, A. J.; Cammi, R.; Pomelli, C.; Ochterski, J. W.; Ayala, P. Y.; Morokuma, K.; Voth, G. A.; Salvador, P.; Dannenberg, J. J.; Zakrzewski, V. G.; Dapprich, S.; Daniels, A. D.; Strain, M. C.; Farkas, O.; Malick, D. K.; Rabuck, A. D.; Raghavachari, K.; Foresman, J. B.; Ortiz, J. V.; Cui, Q.; Baboul, A. G.; Clifford, S.; Cioslowski, J.; Stefanov, B. B.; Liu, G.; Liashenko, A.; Piskorz, P.; Komaromi, I.; Martin, R. L.; Fox, D. J.; Keith, T.; Al-Laham, M. A.; Peng, C. Y.; Nanayakkara, A.; Challacombe, M.; Gill, P. M. W.;

Johnson, B.; Chen, W.; Wong, M. W.; Gonzalez, C.; Pople, J. A. *Gaussian 03*, revision C.02; Gaussian, Inc.: Wallingford, CT, 2004.

(66) Krueger, B. P.; Scholes, G. D.; Fleming, G. R. *J. Phys. Chem. B* **1998**, *102*, 5378.

(67) Schaftenaar, G.; Noordik, J. H. *J. Comput.-Aided Mol. Des.* **2000**, *14*, 123.

(68) Kim, J. Ultrafast Dynamics of Polarons, Excitons and Excitations in Conjugated Molecules. Ph.D. Thesis, The University of Chicago, 2004.

(69) Vöhringer, P.; Scherer, N. F. *J. Phys. Chem.* **1995**, *99*, 2684.

(70) Burget, D.; Jacques, P.; Vauthey, E.; Suppan, P.; Hasselbach, E. *J. Chem. Soc., Faraday. Trans.* **1994**, *90*, 2481.

(71) Gould, I. R.; Farid, S. *Acc. Chem. Res.* **1996**, *29*, 522.

(72) Zhou, J.; Findley, B. R.; Braun, C. L.; Sutin, N. *J. Chem. Phys.* **2001**, *114*, 10448.

(73) Newton, M. D.; Sutin, N. *Annu. Rev. Phys. Chem.* **1984**, *35*, 437.

(74) Zhou, J.; Findley, B. R.; Teslja, A.; Braun, C. L.; Sutin, N. *J. Phys. Chem. A* **2000**, *104*, 11512.

(75) Miller, J. R.; Beitz, J. V.; Huddleston, R. K. *J. Am. Chem. Soc.* **1984**, *106*, 5057.

(76) Moser, C. C.; Keske, J. M.; Warncke, K.; Farid, R. S.; Dutton, P. L. *Nature (London)* **1992**, *355*, 792.

(77) Tavernier, H. L.; Fayer, M. D. *J. Phys. Chem. B* **2000**, *104*, 11541.

(78) Priyadarshy, S.; Risser, S. M.; Beratan, D. N. *J. Phys. Chem.* **1996**, *100*, 17678.

(79) Lapidus, L. J.; Eaton, W. A.; Hofrichter, J. *Phys. Rev. Lett.* **2001**, *87*, 258101.

(80) Zusman, L. D. *Chem. Phys.* **1980**, *49*, 295.

(81) Sumi, H.; Marcus, R. A. *J. Chem. Phys.* **1986**, *4894*, 84.

(82) Hynes, J. T. *J. Phys. Chem.* **1986**, *90*, 3701.

(83) Sparpaglion, M.; Mukamel, S. *J. Chem. Phys.* **1988**, *88*, 3263.

(84) Sparpaglion, M.; Mukamel, S. *J. Chem. Phys.* **1988**, *88*, 4300.

(85) McManis, G. E.; Weaver, M. J. *J. Chem. Phys.* **1989**, *90*, 912.

(86) Bunding, K. A.; Bell, M. I.; Durst, R. A. *Chem. Phys. Lett.* **1982**, *89*, 54.

(87) Bowman, R. M.; Dantus, M.; Zewail, A. H. *Chem. Phys. Lett.* **1989**, *161*, 297.

(88) Scherer, N. F.; Jonas, D. M.; Fleming, G. R. *J. Chem. Phys.* **1993**, *99*, 153.

(89) Kim, Y. R.; Share, P.; Pereira, M.; Sarisky, M.; Hochstrasser, R. M. *J. Chem. Phys.* **1989**, *91*, 7557.

(90) Nagarajan, V.; Johnson, E. T.; Williams, J. C.; Parson, W. W. *J. Phys. Chem. B* **1999**, *103*, 2297.

(91) Book, L. D.; Ostafin, A. E.; Ponomarenko, N.; Norris, J. R.; Scherer, N. F. *J. Phys. Chem. B* **2000**, *104*, 8295.

(92) Ferro, A. A.; Jonas, D. M. *J. Chem. Phys.* **2001**, *115*, 6281.

(93) Min, C. K.; Joo, T.; Yoon, M. C.; Kim, C. M.; Hwang, Y. N.; Kim, D.; Aratani, N.; Yoshida, N.; Osuka, A. *J. Chem. Phys.* **2001**, *114*, 6750.

(94) Varnavski, O. P.; Ostrowski, J. C.; Sukhomlinova, L.; Twieg, R. J.; Bazan, G. C.; Goodson, T., III. *J. Am. Chem. Soc.* **2002**, *124*, 1736.

(95) Debye, P. *Polar Molecules*; Dover: New York, 1929.

(96) Viswanath, D. S.; Natarajan, G. *Data Book on the Viscosity of Liquids*; Hemisphere Publishing Corporation: New York, 1989.

(97) Moran, A. M.; Herschberger, M. A.; Scherer, N. F. Research in progress.

(98) Park, S.; Flanders, B. N.; Shang, X.; Westervelt, R. A.; Kim, J.; Scherer, N. F. *J. Chem. Phys.* **2003**, *118*, 3917.

(99) Bell, I. P.; Rodgers, M. A. J.; Burrows, H. D. *J. Chem. Soc., Faraday Trans. 1* **1977**, *73*, 315.

(100) Xia, C.; Peon, J.; Kohler, B. *J. Chem. Phys.* **2002**, *117*, 8855.

(101) Gumy, J. C.; Nicolet, O.; Vauthey, E. *J. Phys. Chem. A* **1999**, *103*, 10737.